A Proof-of-Concept Study for Precise Mapping of Pigmented Basal Cell Carcinoma in Asian Skin using Multispectral Optoacoustic Tomography Imaging with Level Set Segmentation

[1,+]Xiuting Li, [1,+]Valerie Xinhui Teo, [2]Cheng Yi Kwa, [3]Amalina Binte Ebrahim Attia, [1]Renzhe Bi, [2]Sai Yee Chuah, [2]Melissa Wee Ping Tan, [2]Hui Yi Chia, [2]Sze Hon Chua, [2]Joyce Xiong See Lee, [2]Suzanne Wei Na Cheng, [1]Dinish U. S.[*], [2]Steven Tien Guan Thng[*], [1]Malini Olivo[*]

[1]A*STAR Skin Research Labs (A*SRL), Agency for Science, Technology and Research (A*STAR), 31 Biopolis Way, #07-01 Nanos, Singapore 138669, Republic of Singapore
[2]National Skin Centre, Singapore, Singapore
[3]Biomedical Research Council (BMRC), Agency for Science, Technology and Research (A*STAR), Singapore, Singapore

[+]Joint first authors

*Corresponding authors: dinish@asrl.a-star.edu.sg; malini_olivo@asrl.a-star.edu.sg; steventhng@nsc.com.sg

Abstract

Basal Cell Carcinoma (BCC), the most common subtype of non-melanoma skin cancers (NMSC), is prevalent worldwide and poses significant challenges due to their increasing incidence and complex treatment considerations. Existing clinical approaches, such as Mohs micrographic surgery, are time-consuming and labour-intensive, requiring meticulous layer-by-layer excision and examination, which can significantly extend the duration of the procedure. Current optical imaging solutions also lack the necessary spatial resolution, penetration depth, and contrast for effective clinical use. Here, we introduce photoacoustic imaging, also known as optoacoustic imaging, based Multispectral Optoacoustic Tomography (MSOT) as a promising solution for non-invasive, high-resolution imaging in dermatology, which also measures hemodynamic changes. MSOT offers high isotropic resolution (80 µm), increased tissue penetration, and contrast-enhanced 3D spatial imaging map. For the first time, we integrated an automated level-set image segmentation methodology on optoacoustic images to further enhance the precision in delineating tumor boundaries. Through this proof-of-concept study in 30 subjects, we demonstrate that this segmentation allows for precise measurement of tumor width, depth, and volume, aiding in preoperative tumor mapping and surgical planning. These measurements, validated against histology, achieved a correlation coefficient of 0.84 and 0.81 for width and depth respectively, ensuring reliable tumor metrics with a low margin of error. Clinicians can use these tumor metrics to optimize treatment efficacy, while preserving healthy tissue and cosmetic outcomes. This advancement has the potential to revolutionize diagnostics and treatment, significantly improving the patient outcomes in managing NMSC.

Keywords: Basal Cell Carcinoma, Non-melanoma Skin Cancer, Photoacoustic Imaging, Multispectral Optoacoustic Tomography, Level-Set Image Segmentation.

1. Introduction

Skin, the body's largest organ, uniquely interfaces with the external world, protecting us while reflecting our health, yet remains vulnerable to skin cancer. In recent decades, skin cancer has emerged as a significant public health concern, challenging our perception of safety under the sun. Despite the skin's formidable defence mechanisms, prolonged exposure to ultraviolet radiation, among other risk factors, can trigger genetic mutations leading to the development of various forms of skin cancer[1,2]. Among the main types of skin cancer[3] - melanoma, squamous cell carcinoma (SCC), basal cell carcinoma (BCC) - BCC is the most common subtype of nonmelanoma skin cancer (NMSC) with an estimated 4.3 million diagnosed each year in the United States alone[4].

Yet, within this landscape of skin cancer research, significant gaps remain. Despite the extensive exploration of BCC subtypes[5], much of this research has been conducted primarily on Caucasian skin[6,7,8]. This omission is evident given the escalating incidence of BCC within the Asian[9] population and the documented prevalence of pigmented BCC among them[10]. Although the incidence of NMSC in individuals with coloured skin tones is relatively lower than Caucasian skin, morbidity and mortality rates are often disproportionately higher within these populations[11,12]. This discrepancy emphasizes a critical need for research that accounts for the intricacies in clinical presentation of BCC and characteristics within diverse racial and ethnic groups[13].

Furthermore, traditional methodologies for assessing tumor boundaries, such as histopathology[14], have certain limitations, particularly in the clinical management of BCC in Asia. While histopathological analysis remains essential for accurate diagnosis and treatment planning following a biopsy, the process can be time-consuming and labour-intensive, with turnaround times influenced by the workload of pathology labs. In cases requiring Mohs Micrographic Surgery (MMS), the procedure may be extended, as it necessitates the iterative removal and examination of tissue layers to achieve clear margins. Although effective, these methods rely on invasive procedures and lack real-time imaging capabilities, which could enhance the dynamic monitoring of tumor boundaries. Additionally, the two-dimensional (2D) nature of histopathology slices provides a partial view of the complete three-dimensional (3D) tumor structure, which may limit comprehensive spatial understanding. Moreover, as histopathology is performed on biopsy or post-mortem samples, it doesn't facilitate ongoing real-time monitoring. The subjective nature of image interpretation can also lead to variability in results[15], highlighting the importance of efforts to reduce inter-observer differences and standardize tumor boundary assessments.

Established imaging modalities such as Optical Coherence Tomography (OCT) and Reflectance Confocal Microscopy (RCM) have significantly advanced the field of non-invasive skin cancer imaging. OCT provides high-resolution cross-sectional images of tissue structures[16,17], while RCM offers exceptional cellular level detail[18,19], making them valuable tools for diagnosing and assessing BCC. The penetration depths of RCM (200–300 μm)[20] and OCT (1–2 mm)[17] make them particularly suitable for the interrogation of superficial BCC subtypes, which are confined to the upper dermis. However, in a clinical setting, the typical depth of BCC ranges from 2–3 mm, with infiltrative subtypes occasionally extending to 3–5 mm[21,22]. These depths exceed the penetration capabilities of RCM and OCT, limiting their ability to accurately delineate the deeper boundaries of BCC lesions, which is critical for comprehensive tumor mapping. Additionally, these modalities lack the incorporation of functional microvascular hemodynamic information, such as tissue chromophores or metabolic activity, thereby limiting their ability to comprehensively characterize lesions.

In the context of this application, photoacoustic imaging (PAI) emerges as a promising imaging modality for tumor boundary delineation. PAI's capability of achieving penetration depths within the range of BCC lesions[23,24] and its ability to provide high-resolution imaging makes it well-suited for this purpose. Additionally, it offers both structural and hemodynamic functional information, enabling comprehensive characterization of tumor features. By resolving endogenous absorbers such as oxyhaemoglobin (HbO_2), deoxyhaemoglobin (Hb), melanin, collagen, and lipid, PAI enables precise in vivo studies of tumor angiogenesis or inflammation. Particularly noteworthy is its potential to study pigmented BCC in Asian populations by exploiting melanin contrast[18]. This versatility has propelled the development of hand-held probes incorporated to multispectral optoacoustic tomography (MSOT) imaging system for clinical implementation, offering significant advancements in dermatological research and patient care within clinical settings[25,26]. However, in the abovementioned applications, despite demonstrating high correlations coefficients of up to 0.90 with histology measurements, the manual approach of measuring tumor dimensions introduces the potential for inter-observer variability and is time-consuming. Therefore, addressing existing clinical and optical challenges necessitates the integration of advanced imaging modalities that provide high optical penetration depth, coupled with a robust algorithm for objective interpretation and standardized method of tumor boundary delineation in real-time.

Conventional algorithmic methods, such as edge-based segmentation, rely on variations in image contrast, texture, color, and saturation, while the snake algorithm uses an energy-based approach to guide a curve to the object boundary by minimizing a weighted energy function[27-29]. Although effective in certain cases, these methods face limitations with lower contrast images, complex boundaries, and dynamic topological changes[27-29]. The level set method, introduced by Osher and Sethian[30-32], addresses these challenges by evolving surfaces rather than curves, allowing it to handle images with poorly defined edges and significant topological variation. Widely used in medical imaging, including CT, MRI, and ultrasound[33-37], level set segmentation has demonstrated robustness in complex image analysis. In this study, we apply the level set method to photoacoustic imaging (PAI) for the first time in a clinical setting. By employing the convex relaxation method of the continuous Potts model, as developed by Zach and Lellmann[38,39], we optimize its compatibility with PAI, allowing for precise boundary detection. To the best of our knowledge, this is the first application of level set segmentation on PAI in a clinical setting.

In this proof-of-concept study, we delve into the potential of PAI complemented with an in-house developed level set segmentation algorithm, highlighting its applications in accurate, real-time tumor margin delineation of pigmented BCC lesions. Through this exploration, we aim to highlight the translational potential of this technology in addressing the persistent challenges of lesion boundary delineation, the time-consuming nature of traditional histopathology, and re-excision rate of MMS. Our method has the potential to serve as a complementary tool to histopathology, providing more precise preoperative mapping and surgical planning, which could ultimately improve patient outcomes.

Methods

2.1 Ethics and study population

The clinical study was approved by the Domain Specific Review Board (DSRB) of National Health Group, Singapore (Ref: 2020/00115 and 2022/00347) and the Agency for Science, Technology and Research Institutional Review Board (Ref: 2020-160 and 2022-145).

A total of 65 subjects, aged between 21 and 90 years, and presenting with lesions suspected of NMSC scheduled for excision with margin or MMS, were recruited and consented for the study. Patients who refused surgery were excluded from the study. Prior to surgery, these lesions underwent imaging with MSOT 3D probe. Subsequently, 16 subjects were withdrawn from the study after histological examination revealed no evidence of BCC. After filtering for subjects specifically diagnosed with pigmented BCC, the study cohort was refined to 30 subjects. All subjects were categorized as Fitzpatrick skin types III and IV. Only de-identified data relevant to the analysis were sent to the team at A*STAR. The patient demographics are presented in Table 1.

	Number of subjects (n=30)
Age (years)	
Mean ± SD	71.3 ± 9.26
Min - Max	55 - 88
Median	72
Sex	
Male	20 (66.6%)
Female	10 (33.3%)
Race	

Caucasian	1 (0.03%)
Chinese	27 (90.0%)
Malay	1 (0.03%)
Others	1 (0.03%)

Table 1. Demographics and characteristics of patients with pigmented BCC (n=30).

1.2 Histology

All the excised skin lesions were examined histologically using the standard stain with haematoxylin and eosin (H&E).

2.3 MSOT system and imaging protocol

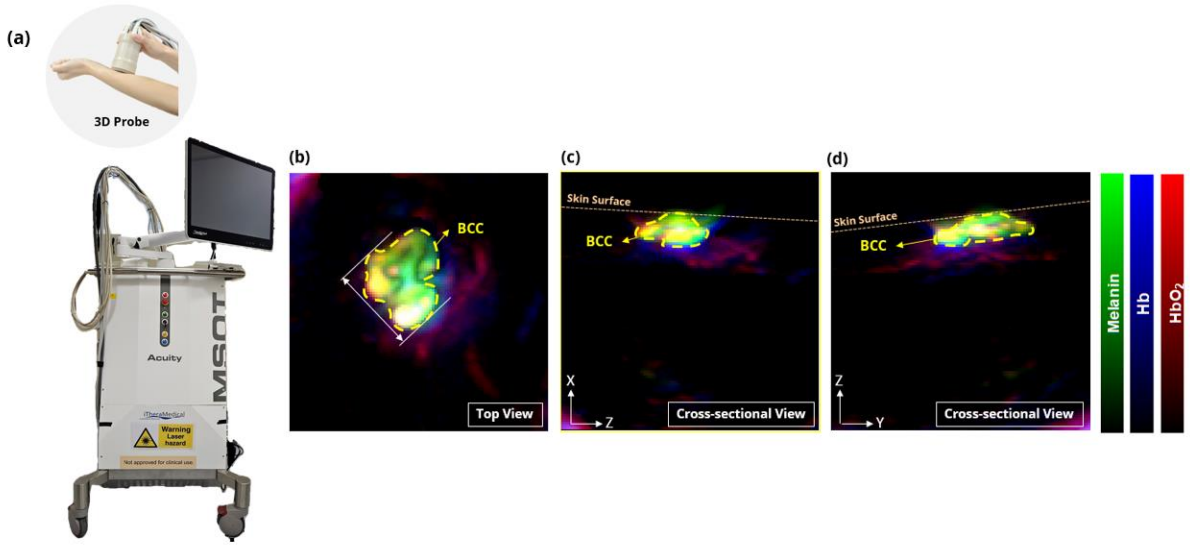

Figure 1. MSOT system and multi-channel 3D images. (a) MSOT Acuity system and handheld 3D probe. (b) x-y plane (tumor width). (c) x-z plane (tumor depth). (d) z-y plane (tumor depth) spectral unmixed for 3 tissue chromophores (melanin, Hb, and HbO_2).

The system used in this study is the MSOT Acuity system (iThera Medical GmbH, Germany), coupled with a 3D handheld probe for in vivo imaging of the lesion, as depicted in Figure 1a. The MSOT system operates within a wavelength range of 680 to 980 nm, with a repetition rate of 10 Hz and an energy output of 10 mJ at 730 nm. It offers a resolution of 80 µm and a field-of-view measuring 15 mm x 15 mm, with a penetration depth of up to 10 mm. Spectral unmixing within the wavelength region of 680 to 920 nm detects endogenous chromophores of melanin, Hb, and HbO_2 as illustrated in Figure 1b to 1d.

The imaging protocol involves begins with the patient completing a consent form obtaining consent from the patient, followed by the capture of dermascopic and clinical photographs of the lesion as part of clinical routine. Subsequently, MSOT imaging commences, beginning with the system setup and parameter configuration. Safety goggles are worn by all individuals present in the imaging room, including the patient. The handheld probe is cleaned, disinfected, and applied to the region of interest (ROI) with ultrasound gel acting as a coupling agent. Image preview is initiated to assess real-time image quality, with probe adjustment performed as needed to optimize imaging of the BCC. After data acquisition, the handheld probe is removed, and residual ultrasound gel is cleaned off from the ROI and the probe. Raw data is then utilized for image reconstruction and spectral unmixing.

Following MSOT imaging, a surgical pen is used to mark the location of measurements on the skin to ensure accurate localization for subsequent biopsy procedures. A 3D image comprising 100 x 100 x 100 pixels with three channels (HbO_2, Hb, and melanin) is obtained after measurements. The image acquisition process took approximately 2 to 5 minutes.

2.4 MSOT image processing

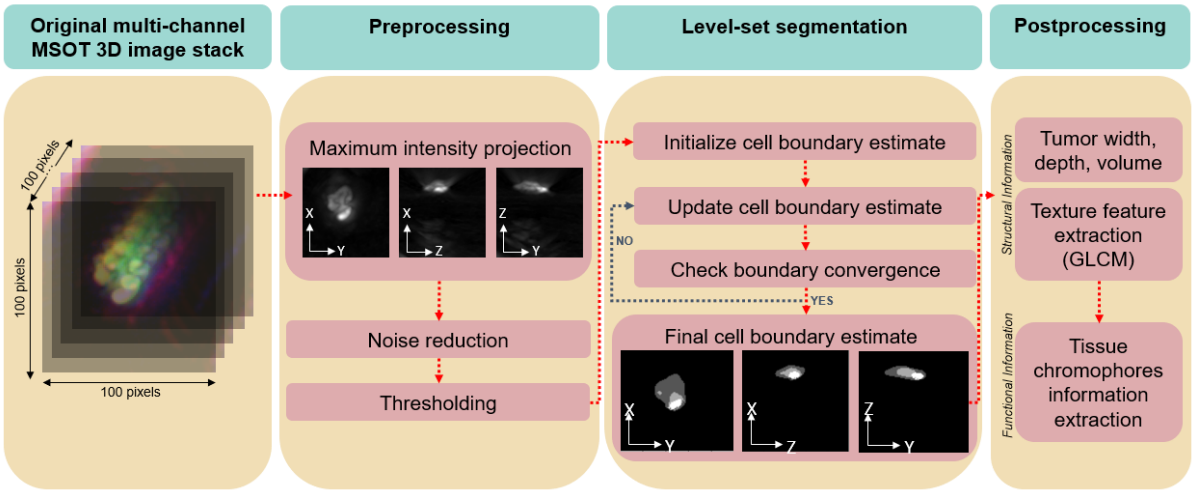

Figure 2. Image analysis workflow. This figure demonstrates the initial 3D image stack obtained from MSOT to the final structural and hemodynamic functional information obtained after analysis.

The image processing workflow consists of pre-processing, level-set segmentation, and post-processing stages as illustrated in Figure 2. The algorithmic sequence starts with pre-processing steps designed to improve visualization and reduce noise in the PA images. We initialize the contour using the contrast gradient of the intensity map from these images. A level-set model is then applied, integrating both region partitioning and constrained boundary information to enable robust and precise boundary detection. This approach enables accurate measurements of tumor size and volume, along with effective extraction of texture features. The detailed procedures for each stage are given below.

i. *Preprocessing*

The 3D image acquired from MSOT's melanin channel undergoes initial processing steps to enhance visualization and reduce noise. Firstly, the 3D image is projected onto three 2D planes (x-y, x-z, y-z) using maximum intensity projection. This technique involves selecting the pixel with the highest intensity value along each line of sight to create a 2D representation of the structure within the 3D volume. Then, the resulting 2D images undergo noise reduction using a median filter, which effectively suppresses random variations in intensity caused by noise. Additionally, a 20% threshold of the maximum intensity is applied to further enhance image clarity and delineate features of interest.

ii. *Level Set Segmentation*

Subsequently, level set segmentation is employed on the three 2D projections to delineate the boundaries of pigmented BCC lesions. The algorithm undergoes multi-partitioning and multi-labelling, based on a convex relaxation of the continuous Potts model[38-40], iteratively using the curve of the level set function over time to compute the optimal partitions and accurately adapt to the object boundaries.

$$\min_{\{\emptyset_{i-1}^{N},\boldsymbol{C}\}} \sum_{i=1}^{N} \int_{\emptyset_i} |I - c_i|^{\gamma} dx + \lambda \sum_{i=1}^{N} |\partial \emptyset_i| \quad (1)$$

$$\bigcup_{i=1}^{N} \varphi_i = \emptyset \ , I_{\varphi_i}(x) = \begin{cases} 1, & x \in \varphi_i \\ 0, & x \notin \varphi_i \end{cases}, \ i = 1,2, \dots, N \tag{2}$$

$$f_i = |I - c_i|^{\gamma} \tag{3}$$

The energy function in Equation 1 is composed of the sum of multi-partition and the boundary lengths of these partitions. Here, $\boldsymbol{I}$ represent the input image, which is divided into N disjoint partitions φ_i , φ_i denote the characteristic functions of the disjoint subdomains with constrains listed in Equation 2, $\boldsymbol{C} = \{c_1, c_2, .. c_N\}$ are the constants for the initialization. The level set function $f_i = |I - c_i|^{\gamma}$ can have coefficients $\gamma = 1 \ or \ 2$ and λ can be adjusted to find the optimal partitions. The boundary lengths of the subdomains are given by $\partial\emptyset_i$. By minimizing the energy function, the level set function f_i (Equation 3) evolves to fit the optimal object boundary.

The segmentation process begins with initializing an estimate of the cell boundary into N=5 disjoint subdomains, with initial constraints c_i incorporating intensity thresholds corresponding to 0%, 20%, 40%, 60%, and 80% of the maximum intensity within the images. The level set function f_i is used to iterate the evolving surface of the tumor to separate it from the background signals. Subsequently, it is iteratively updated to minimize the energy function that quantifies the difference between the evolving boundary and the actual boundary of the lesion. At each iteration, the convergence of the boundary estimate is checked against the convergence of the energy function. Once convergence is achieved, the final cell boundary estimate is obtained, providing an accurate representation of the BCC lesion morphology within the MSOT images.

iii. Post-processing

With the acquisition of precisely segmented images, the dimensions of the tumor can be accurately computed. The Maximum Feret's Diameter (MFD) was employed to determine the tumor width, a method which measures the longest distance between any two parallel tangential lines along the tumor boundary. The tumor depth was measured using the minor axis derived from Python regionprops. This method accounts for the orientation of the tumor within the image, providing a reliable estimation of its depth. To obtain the volume and 3D reconstruction of the image, all 2D slices in each plane are vectorized. Subsequently, the regionprops function is used to calculate the volume of the entire refined 3D tumor reconstruction. Moreover, to enhance visualization and facilitate further analysis, the reconstructed 3D model was saved in an HTML file format, allowing for interactive viewing and rotation.

Gray Level Co-Occurrence Matrix (GLCM), a texture analysis technique, was also applied to the MSOT images to extract qualitative properties such as contrast, dissimilarity, homogeneity, energy, and correlation by quantifying the spatial distribution of pixel intensity values within an image. Contrast measures the local variations in pixel intensity, providing insight into the sharpness of image features. Dissimilarity quantifies the average difference in intensity between neighbouring pixels, reflecting the heterogeneity of the image texture. Homogeneity assesses the uniformity of pixel intensity values, indicating the level of smoothness or coarseness in the image texture. Energy represents the uniformity of pixel pairs, with higher values indicating a more homogeneous texture. Finally, correlation measures the linear dependency between pixel intensities at different locations, offering information about the spatial relationships within the image. From GLCM analysis, texture characteristics of the MSOT images were obtained for interpretation and characterization of pathological features.

2.5 Statistical analysis

Pearson's correlation coefficient and its associated p-value were used to assess the association between tumor dimensions (width and depth) obtained from MSOT algorithm measurements and histology for identical tumors. The calculation of Pearson's correlation coefficient is depicted in Equation 4.

$$r = \frac{\Sigma(x-\bar{x})(y-\bar{y})}{\sqrt{\Sigma(x-\bar{x})^2\Sigma(y-\bar{y})^2}} \quad (4)$$

where x is the histology measurement, $\bar{x}$ is the mean of x, y is MSOT measurement, $\bar{y}$ is the mean of y.

The difference between the actual histology measurements and the MSOT algorithm measurements were also computed as the Margin of Error (MOE) as illustrated in Equation 5. When developing and validating new diagnostic tools or methods, the margin of error is a critical clinical metric. It measures the discrepancy between estimated and actual measurements, providing insight into the accuracy and reliability of algorithms, in our case, level-set segmentation. Understanding and minimizing this margin of error is crucial for ensuring that the algorithmic delineation meet clinical standards and can be effectively integrated into practice. MOE also helps in refining the algorithm and understanding their limitations in clinical practice.

$$\text{MOE} = \text{y-x} \quad (5)$$

where x is the histology measurement, y is MSOT measurement.

The mean and standard deviation were also computed for the MOE's central tendency and variability of the discrepancies of all 30 subjects. The mean provides an average measure of the MOE, indicating the typical magnitude of the segmentation error, while the standard deviation reflects the extent to which these errors vary around the mean, offering insight into the consistency and reliability of the segmentation method.

2. Results

3.1 Comparison with histology measurements

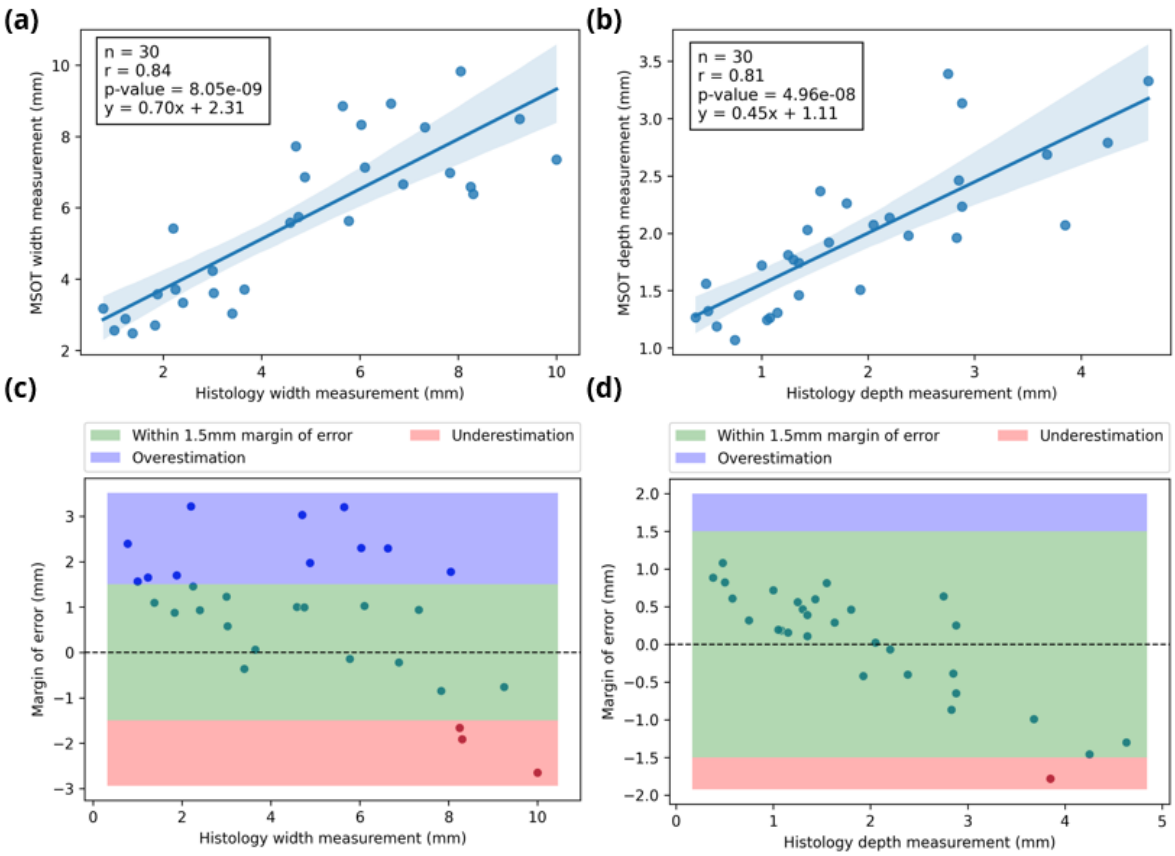

Figure 3. Comparison of MSOT-obtained measurements with histology. Correlation of tumor (a) width and (b) depth between MSOT and histology measurements. Translucent band around the regression line is the 95% confidence interval for the regression estimate. Margin of error between MSOT and histology (c) width and (d) depth measurements set to be within 1.5 mm.

The MSOT measurements of tumor width and depth were compared with the gold standard histology measurements as shown in Figure 3a and 3b. The correlation between MSOT and histology measurements obtained were 0.84 (p-value: 8.05 X 10^{-9}) and 0.81 (p-value: 4.96 X 10^{-8}) respectively. Importantly, the 95% confidence intervals were compact and closely aligned with the estimated regression line, particularly for smaller tumor dimensions.

MOE between MSOT measurements of tumor width and depth were compared with the gold standard histology measurements as shown in Figure 3c and 3d. 1.5 mm was taken to be the clinical MOE in this study which reflects the level of precision generally acceptable in clinical practice for tumor margin assessment[41,42]. 51% and 96% of our subjects were within the 1.5 mm MOE for width and depth measurements respectively. If the MOE is larger than 1.5 mm, the measurement is considered an overestimation (blue fill). If the MOE is smaller than -1.5 mm, the measurement is considered an underestimation (red fill). For the width MOE, the mean was calculated to be 0.89 mm with a standard deviation of 1.47 mm. In contrast, the depth MOE exhibited a mean of 0.043 mm with a standard deviation of 0.74 mm.

3.2 Case Study

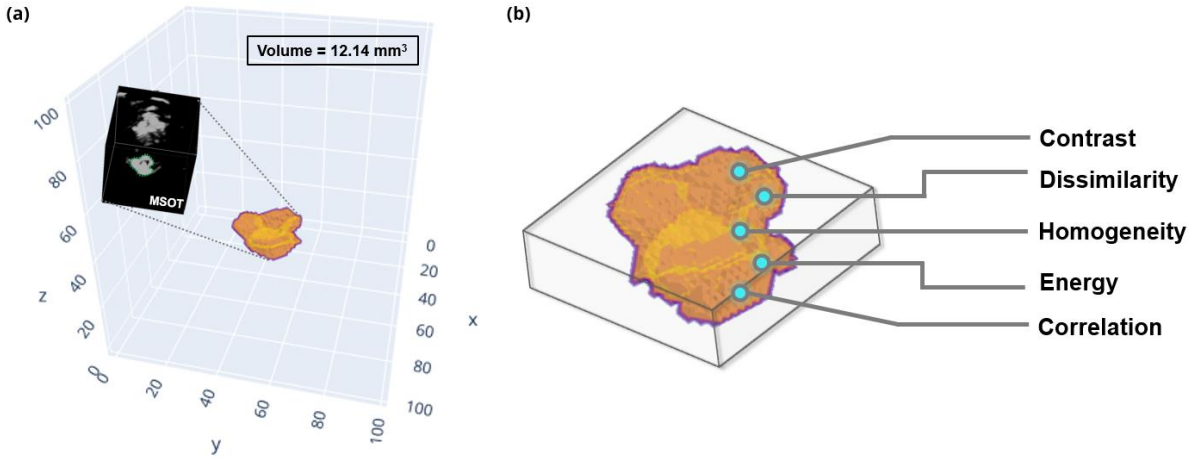

Figure 4. Case study of quantitative features for future investigations. (a) 3D reconstruction of segmented 2D BCC slices to obtain volume of tumor in comparison with original MSOT 3D render (black cube). (b) Quantitative properties of the tumor obtained from Gray Level Co-occurrence Matrix algorithm.

In a case study of Subject 36, the 2D processed images were further reconstructed to a 3D image as shown in Figure 4a. From the 3D image, the volume of the tumor can be obtained from the constructed mesh of the tumor to obtain a volume of 12.14 mm^3. Compared to the original 3D rendering of the tumor using MSOT, the reconstructed image has significantly less noise and artefacts.

Utilizing the same subject as a case study, various quantitative properties including contrast, dissimilarity, homogeneity, energy, and correlation can be extracted, as illustrated in Figure 4b. These properties are computed across all three 2D planes encompassing the tumor. The resulting averages for these calculations are as follows: contrast (28.46), dissimilarity (1.99), homogeneity (0.64), energy (0.21), and correlation (0.98).

The hemodynamic functional characteristics of the tumor, including melanin, oxyhaemoglobin, deoxyhaemoglobin, collagen, and lipid content, can also be qualitatively assessed through the various MSOT channels, as depicted in Figures 1b to 1g. While these channels offer insights into relative changes or ratios of photoacoustic signals, enabling the identification of variations between diseased and healthy tissues, this study does not delve deeply into their exploration.

4. Discussion

The present study was designed to address the existing challenges of tumor boundary delineation of photoacoustic images by incorporating a novel robust segmentation algorithm. This workflow demonstrated promising results, with a strong correlation coefficient of 0.84 for tumor width and 0.81 for tumor depth when compared to the established clinical gold standard of histopathology. Upon closer examination, it was noted that when computing the MOE, the algorithm exhibited a tendency to slightly overestimate the width of smaller tumors while underestimating those of larger tumors. Nevertheless, over 51% and 96% of width and depth measurements, respectively, fell within an acceptable range of 1.5 mm MOE, suggesting consistent performance across various tumor sizes. The mean MOE for width (0.89 mm) demonstrates that the level-set segmentation method achieves a reasonably close approximation to the actual histology measurements, typically deviating by less than 1 mm. The standard deviation of 1.47 mm reflects some variability in width measurements across different subjects, suggesting opportunities for further optimization in width estimation. In contrast, the depth MOE exhibited a small mean of 0.043 mm, highlighting the method's high accuracy in estimating tumor depth with minimal error. The standard deviation of 0.74 mm, though lower than that of the width MOE, further supports the method's consistency in depth estimation, confirming its reliability and effectiveness in this dimension.

These findings highlight the capabilities of the proposed methodology to streamline the subjective diagnostic assessment of tumor boundaries, representing a notable advancement over previous approaches where tumor dimensions were manually measured after the conversion of 3D MSOT images into 2D[25,26,43] By leveraging a robust segmentation algorithm, this novel methodology offers the advantage of eliminating inter-observer variability, ensuring greater consistency and reliability in the delineation of tumor boundaries. Moreover, the entire process from image acquisition to image processing is completed within 20 minutes which is a stark contrast to the conventional clinical practices in Singapore, where the combined process of biopsy, histopathological analysis, and MMS can take several days. The extended duration not only increases the overall treatment costs but also delays critical treatment decisions. This streamlined process not only boost the efficiency of diagnostic procedures but also encourage more precise treatment planning and monitoring.

Breslow thickness stands as the foremost prognostic factor in current clinical practice[44], providing critical insight into disease progression. With our algorithmic workflow, we can capture this essential information. Moreover, it's important to note that tumor width and depth, while valuable, represent unidimensional measurements, offering limited perspective on tumor characteristics. Recognizing the significance of comprehensive tumor assessment, recent studies have highlighted the potential utility of tumor volume as an additional feature for cancer staging[44,45]. By incorporating tumor volume into prognostic assessments, we propose a potentially valuable predictor of disease outcome. This expansion of prognostic factors could enhance our ability to stratify patients more accurately, leading to more tailored treatment strategies and ultimately improving clinical outcomes.

The capability to also generate detailed and precise 3D map of the tumor as shown in our case study, serves as a valuable tool for clinicians in several ways, particularly in preoperative mapping and surgical planning. This functionality also provides researchers and clinicians with a versatile tool for detailed examination and interpretation of the tumor' s volumetric features. By providing a comprehensive visualization of the tumor size, and shape, this technology enables clinicians to strategize and optimize surgical interventions with enhanced accuracy and confidence. Preoperative mapping using these refined 3D maps allows surgeons to delineate the extent of the tumor, facilitating the development of precise surgical approaches and minimizing the risk of inadvertent damage to healthy tissues. Additionally, surgeons can simulate various surgical scenarios and anticipate potential challenges leading to more efficient procedures.

The textural information extracted through GLCM analysis in our case study highlights the potential to capture additional quantitative details about the tumor's structure beyond mere dimensions. These metrics enhance interpretation and characterization of pathological features, potentially aiding in the differentiation of tumor subtypes and informing treatment strategies by correlating with tumor aggressiveness and stage. Combined with the quantitative hemodynamic functional data achievable through our workflow, this approach could provide a more comprehensive assessment of the tumor and its response to therapy. These insights could lead to more personalized treatment plans, optimizing therapeutic outcomes and minimizing unnecessary interventions. We aim to explore these insights further in the ongoing prospective studies involving a larger cohort. Further investigations in our study with an expanded sample size are warranted to substantiate these findings in this field. By leveraging machine learning classification, we intend to categorize subjects into various BCC subtypes, enhancing our understanding of the disease's heterogeneity and aiding in more precise diagnosis and treatment planning.

Looking ahead, we aim to integrate machine learning classification algorithms to include tumor subtype classification and cancer staging by incorporating quantitative information regarding both the structural and hemodynamic functional characteristics of the tumor. Additionally, other MSOT image channels can be leveraged to segment non-pigmented BCC cases, further expanding the applicability and effectiveness of the approach in diverse clinical scenarios. We also aim to reduce the margin of error to 1 mm by applying machine learning techniques to determine the initial cell boundary state for the level set function, thereby making the algorithm more robust.

5. Conclusion

In this proof-of-concept study, we have demonstrated the effectiveness of utilizing the combination of MSOT with a robust level-set segmentation algorithm to achieve precise tumor boundary delineation, particularly in determining the margins of pigmented BCC in the Asian population. Through a pilot clinical study, over 80% correlation with histology measurements was achieved, emphasizing the reliability and accuracy of this approach. Furthermore, this integrated methodology not only provides tumor dimensions but also offers insights into the textural characteristics and tumor volume and 3D map, thereby enhancing our understanding of its pathophysiology. Notably, the ability to complete the entire process within 20 minutes represents a significant advantage over conventional methods, drastically reducing the time needed for diagnosis and treatment planning, and offering quicker, more efficient patient care. Overall, these findings highlight the potential of this innovative approach to transform clinical practice by providing rapid, accurate tumor characterization, ultimately leading to improved diagnostic and therapeutic outcomes for patients with skin cancer.

Acknowledgement

This work was supported by the Industry Alignment Fund Pre-positioning Programme (IAFPP), Award H19H6a0025, which provided crucial funding to facilitate the alignment of our research objectives. Additionally, we received significant support from the A*STAR Biomedical Research Council (BMRC) Central Research Fund (2024), which was instrumental in advancing our research. The authors would also like to express their gratitude for the invaluable support and collaboration under the joint lab agreement with iThera Medical.

Funding

This work was supported by industry alignment fund pre-positioning programme, Award H19H6a0025 and A*STAR BMRC Central Research Fund (2024).

Data Availability Statement

No large datasets were generated in these studies.

Author Contributions

The conceptualization of the study was carried out by Xiuting Li, Valerie Teo Xinhui, and U. S. Dinish, Steven Tien Guan Thng, and Malini Olivo. Data curation and patient recruitment was managed by Kwa Cheng Yi, Amalina Binte Ebrahim Attia, Chuah Sai Yee, Melissa Tan Wee Ping, Chia Hui Yi, Chua Sze Hon, Joyce Lee Xiong See, and Suzanne Cheng Wei Na, Bi. Renzhe and Steven Thng. Xiuting Li, Valerie Teo Xinhui, U. S. Dinish were responsible for the formal analysis, investigation, methodology, and software development. Xiuting Li and Valerie Teo Xinhui and U. S. Dinish interpreted the data obtained. The original draft of the manuscript was prepared by Xiuting Li, Valerie Teo Xinhui, while Bi Renzhe and U. S. Dinish, Steven Thng contributed to the review and editing of the manuscript. Supervision was provided by U. S. Dinish, Steven Tien Guan Thng, and Malini Olivo.

Declarations

Competing interest

The authors declare no competing interests.

Ethics approval

The clinical study was approved by the Domain Specific Review Board (DSRB) of National Health Group, Singapore and the Agency for Science, Technology and Research Institutional Review Board (IRB).

DSRB Ref: 2020/00115 and 2022/00347

A*STAR IRB Ref: 2020-160 and 2022-145

Consent to participate

Informed consent was obtained from all individual participants included in the study.

References

1. MPH, CPH & Saladi, Rao & MD, FAAD. (2010). Review: Ultraviolet radiation and skin cancer. International Journal of Dermatology. 49. 978 - 986. 10.1111/j.1365-4632.2010.04474.x.
2. Nakazawa, H & English, Dallas & Randell, P & Nakazawa, K & Martel, Nicole & Armstrong, B & Yamasaki, Hiroshi. (1994). UV and skin cancer: specific p53 gene mutation in normal skin as a biologically relevant exposure measurement. Proceedings of the National Academy of Sciences of the United States of America. 91. 360-4. 10.1073/pnas.91.1.360.
3. Lee, Peter. (2004). Common skin cancers. Minnesota medicine. 87. 44-7.
4. Basal & Squamous Cell Skin Cancer Statistics. (n.d.). American Cancer Society. https://www.cancer.org/cancer/types/basal-and-squamous-cell-skin-cancer/about/key-statistics.html
5. Dourmishev, Lyubomir & Rusinova, Darena & Botev, Ivan. (2013). Clinical variants, stages, and management of basal cell carcinoma. Indian Dermatology Online Journal. 4. 12-17. 10.4103/2229-5178.105456.
6. Szeimies, Rolf-Markus & Ibbotson, Sally & Murrell, Dédée & Rubel, D & Frambach, Yvonne & Berker, Dorukhan & Dummer, R & Kerrouche, Nabil & Villemagne, H. (2008). A clinical study comparing methyl aminolevulinate photodynamic therapy and surgery in small superficial basal cell carcinoma (8-20 mm), with a 12-month follow-up. Journal of the European Academy of Dermatology and Venereology: JEADV. 22. 1302-11. 10.1111/j.1468-3083.2008.02803.x.
7. Tangrea, Joseph & Edwards, Brenda & Taylor, Philip & Hartman, Anne & Peck, Gary & Salasche, Stuart & Menon, Padman & Benson, Paul & Mellette, J.Ramsey & Guill, Marshall. (1992). Long-Term Therapy With Low-Dose Isotretinoin for Prevention of Basal Cell Carcinoma: A Multicenter Clinical Trial. Journal of the National Cancer Institute. 84. 328-32. 10.1093/jnci/84.5.328.
8. Venables, Zoe & Nijsten, Tamar & Wong, K.F. & Autier, P. & Broggio, John & Deas, A. & Harwood, Catherine & Hollestein, Loes & Langan, Sinead & Morgan, Eileen & Proby, Charlotte & Rashbass, Jem & Leigh, I.M.. (2019). Epidemiology of basal and cutaneous squamous cell carcinoma in the United Kingdom 2013-2015: a cohort study. British Journal of Dermatology. 181. 10.1111/bjd.17873.
9. Choon Chiat, Oh & Jin, Aizhen & Koh, Woon-Puay. (2021). Trends of cutaneous basal cell carcinoma, squamous cell carcinoma, and melanoma among the Chinese, Malays, and Indians in Singapore from 1968-2016. JAAD International. 4. 39-45. 10.1016/j.jdin.2021.05.006.
10. Kikuchi, A & Shimizu, H & Nishikawa, Takeji. (1996). Clinical histopathological characteristics of basal cell carcinoma in Japanese patients. Archives of dermatology. 132. 320-4. 10.1001/archderm.132.3.320.
11. Battie C, GoharaM, VerschooreM, and Roberts W. Skin cancer in skin of color: an update on current facts, trends, and misconceptions. J Drugs Dermatol 2013;12:194–8.
12. Gupta, Alpana & Bharadwaj, Mausumi & Mehrotra, Ravi. (2016). Skin Cancer Concerns in People of Color: Risk Factors and Prevention. Asian Pacific journal of cancer prevention: APJCP. 17. 6157-6164. 10.22034/APJCP.2016.17.12.6157.
13. Tan, Eugene & Ee, Melvin & Shen, Liang & Chua, Hilary & Chan, Yiong & Tan, Suat-Hoon. (2014). Basal cell carcinoma in Singapore: A prospective study on epidemiology and clinicopathological characteristics with a secondary comparative analysis between Singaporean Chinese and Caucasian patients. Australasian Journal of Dermatology. 56. 10.1111/ajd.12202.
14. Mete, Mutlu & Xu, Xiaowei & Fan, Chun-Yang & Shafirstein, Gal. (2007). Automatic Delineation of Malignancy in Histopathological Head and Neck Slides. BMC bioinformatics. 8 Suppl 7. S17. 10.1186/1471-2105-8-S7-S17.
15. Weltens, Caroline & Menten, Johan & Feron, Michel & Bellon, Erwin & Demaerel, Philippe & Maes, Frederik & Bogaert, Walter & Schueren, Emmanuel. (2001). Interobserver variations in gross tumor volume delineation of brain tumors on computed tomography and impact of magnetic resonance imaging. Radiotherapy and oncology: journal of the European Society for Therapeutic Radiology and Oncology. 60. 49-59. 10.1016/S0167-8140(01)00371-1.
16. Jerjes, Waseem & Sultan, Ahmed & Hopper, Colin. (2016). Image-Guided Surgery by OCT and Other Optical Imaging Modalities. 10.1007/978-1-4939-1758-7_38.
17. Ulrich, Martina. (2016). Optical coherence tomography for diagnosis of basal cell carcinoma: essentials and perspectives. British Journal of Dermatology. 175. 1145-1146. 10.1111/bjd.15137.
18. Malvehy, Josep & Barreiro-Capurro, Alicia & Carrera, Cristina & Puig, Susana. (2016). The Role of Reflectance Confocal Microscopy in Clinical Trials for Tumor Monitoring. Dermatologic Clinics. 34. 10.1016/j.det.2016.06.001.

19. Lupu, Mihai & Popa, Maria & Voiculescu, Vlad & Boda, Daniel & Caruntu, Constantin & Zurac, Sabina & Giurcaneanu, Calin. (2019). A Retrospective Study of the Diagnostic Accuracy of In Vivo Reflectance Confocal Microscopy for Basal Cell Carcinoma Diagnosis and Subtyping. Journal of Clinical Medicine. 8. 449. 10.3390/jcm8040449.
20. Schwartz, Michelle & Siegel, Daniel & Markowitz, Orit. (2016). Commentary on the Diagnostic Utility of Non-invasive Imaging Devices for Field Cancerization. Experimental Dermatology. 25. 10.1111/exd.13103.
21. Pyne, John & Myint, Esther & Barr, Elizabeth & Clark, Simon & Hou, Ruihang. (2018). Basal cell carcinoma: variation in invasion depth by subtype, sex, and anatomic site in 4,565 cases. Dermatology practical & conceptual. 8. 314-319. 10.5826/dpc.0804a13.
22. Wetzel, Megan & Strickley, John & Haeberle, M & Brown, Timothy. (2019). Depth of Invasion of Aggressive and Nonaggressive Basal Cell Carcinoma. The Journal of clinical and aesthetic dermatology. 12. 12-14.
23. Xosé Luís Deán-Ben, Daniel Razansky. (2013) Functional optoacoustic human angiography with handheld video rate three-dimensional scanner. Photoacoustics. Volume 1, Issues 3–4. Pages 68-73. ISSN 2213-5979.
24. Lin, L., Hu, P., Shi, J., Appleton, C., Maslov, K., Li, L., Zhang, R., & Wang, L. (2018). Single-breath-hold photoacoustic computed tomography of the breast. Nature Communications, 9. https://doi.org/10.1038/s41467-018-04576-z.
25. Chuah, S. & Attia, Amalina & Long, Valencia & Ho, Chris Jun Hui & Malempati, Pinky & Fu, C. & Ford, Steven & Lee, J. & Tan, W. & Razansky, Daniel & Olivo, Malini & Thng, Guan Steven. (2016). Structural and functional 3D mapping of skin tumors with non-invasive multispectral optoacoustic tomography. Skin Research and Technology. 23. 10.1111/srt.12326.
26. Attia, Amalina & Chuah, Sai & Razansky, Daniel & Ho, Chris Jun Hui & Malempati, Pinky & U. S, Dinish & Bi, Renzhe & Fu, C.Y. & Ford, Steven & Lee, Joyce & Tan, Melissa & Olivo, Malini & Thng, Guan Steven. (2017). Noninvasive real-time characterization of non-melanoma skin cancers with handheld optoacoustic probes. Photoacoustics. 7. 10.1016/j.pacs.2017.05.003.
27. snake active contour model 1987 2, (n.d.).
28. S. Karthick, K.S. Professor, A. Puraneeswari, A Survey Based on Region Based Segmentation, International Journal of Engineering Trends and Technology 7 (2014). http://www.ijettjournal.org.
29. M. Jacob, T. Blu, M. Unser, Efficient energies and algorithms for parametric snakes, IEEE Transactions on Image Processing 13 (2004). https://doi.org/10.1109/TIP.2004.832919.
30. Osher, Stanley & Sethian, James. (1988). Fronts propagating with curvature-dependent speed: Algorithms based on Hamilton-Jacobi formulations. Journal of Computational Physics. 79. 12-49. 10.1016/0021-9991%2888%2990002-2.
31. Osher, Stanley & Shu, Chi-Wang. (1991). High-Order Essentially Nonoscillatory Schemes for Hamilton–Jacobi Equations. Siam Journal on Numerical Analysis - SIAM J NUMER ANAL. 28. 10.1137/0728049.
32. D.F. (David F.) Parker, Fields, flows, and waves : an introduction to continuum models, Springer, 2003.
33. V. Klement, T. Oberhuber, D. Ševčovič, Application of the level-set model with constraints in image segmentation, (2011). http://arxiv.org/abs/1105.1429.
34. J. Park, S. Park, W. Cho, Medical image segmentation using level set method with a new hybrid speed function based on boundary and region segmentation, IEICE Trans Inf Syst E95-D (2012) 2133–2141. https://doi.org/10.1587/transinf.E95.D.2133.
35. Y. Yin, H. Luo, J. Sa, Q. Zhang, Study and application of improved level set method with prior graph cut in PCB image segmentation, Circuit World 46 (2020) 55–64.
36. Y. Yang, Y. Yang, S. Zhong, Multi-phase level set method for precise segmentation and correction of brain MRI, Signal Image Video Process 15 (2021) 53–61.
37. Z. Wang, B. Ma, Y. Zhu, Review of level set in image segmentation, Archives of Computational Methods in Engineering 28 (2021) 2429–2446.
38. J. Lellmann, J. Kappes, J. Yuan, F. Becker, C. Schnörr, Convex Multi-Class Image Labeling by Simplex-Constrained Total Variation, 2008. http://ipa.iwr.uni-heidelberg.de/.
39. C. Zach, D. Gallup, J.-M. Frahm, M. Niethammer, Fast Global Labeling for Real-Time Stereo Using Multiple Plane Sweeps, 2008.
40. E. Bae, J. Yuan, X.C. Tai, Global minimization for continuous multiphase partitioning problems using a dual approach, Int J Comput Vis 92 (2011) 112–129. https://doi.org/10.1007/s11263-010-0406-y.
41. EPSTEIN, ERNST. (1973). How Accurate is the Visual Assessment of Basal Carcinoma Margins?. British Journal of Dermatology. 89. 37 - 43. 10.1111/j.1365-2133.1973.tb01915.x.

42. Katz, Ian & Irwig, Les & McGeehan, Kevin & Bell, Katy. (2021). I need an exact margin measurement for this basal cell carcinoma!. Journal of Clinical Pathology. 75. jclinpath-2021. 10.1136/jclinpath-2021-208030.
43. Chuah SY, Attia ABE, Ho CJH, Li X, Lee JS, Tan MWP, Yong AA, Tan AWM, Razansky D, Olivo M, Thng STG. Volumetric Multispectral Optoacoustic Tomography for 3-Dimensional Reconstruction of Skin Tumors: A Further Evaluation with Histopathologic Correlation. J Invest Dermatol. 2019 Feb;139(2):481-485. doi: 10.1016/j.jid.2018.08.014. 2018 Sep 15. PMID: 30227137.
44. Voss, Barbara & Wilop, Stefan & Jonas, Stephan & El-Komy, Mohamed & Schaller, Jörg & Felbert, Verena & Megahed, Mosaad. (2013). Tumor Volume as a Prognostic Factor in Resectable Malignant Melanoma. Dermatology (Basel, Switzerland). 228. 10.1159/000356121.
45. Friedman, Robert & Rigel, Darrell & Kopf, Alfred & Grin, Caron & Heilman, Edward & Bart, R & Kamino, Hideko & Harris, Matthew & Roses, Daniel & Postel, Allen. (1991). Volume of malignant melanoma is superior to thickness as a prognostic indicator. Preliminary observation. Dermatologic clinics. 9. 643-8. 10.1016/S0733-8635(18)30368-1.